ACS APPLIED MATERIALS & INTERFACES

Research Article

www.acsami.org

Combination of Magnetic and Enhanced Mechanical Properties for Copolymer-Grafted Magnetite Composite Thermoplastic Elastomers

Feng Jiang,[†] Yaqiong Zhang,[†] Zhongkai Wang,[†] Wentao Wang,[†] Zhaohua Xu,[‡] and Zhigang Wang*[,†]

[†]CAS Key Laboratory of Soft Matter Chemistry, Department of Polymer Science and Engineering, Hefei National Laboratory for Physical Sciences at the Microscale, University of Science and Technology of China, Hefei, Anhui Province 230026, P. R. China

[‡]Department of Material Technology, Jiangmen Polytechnic, Jiangmen, Guangdong Province 529090, P. R. China

Supporting Information

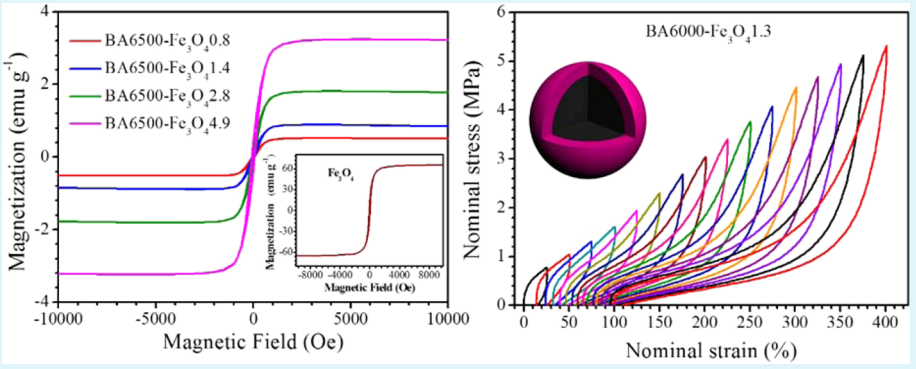

ABSTRACT: Composite thermoplastic elastomers (CTPEs) of magnetic copolymer-grafted nanoparticles (magnetite, Fe_3O_4) were synthesized and characterized to generate magnetic CTPEs, which combined the magnetic property of Fe_3O_4 nanoparticles and the thermoplastic elasticity of the grafted amorphous polymer matrix. Fe_3O_4 nanoparticles served as stiff, multiple physical cross-linking points homogeneously dispersed in the grafted poly(*n*-butyl acrylate-*co*-methyl methacrylate) rubbery matrix synthesized via the activators regenerated by electron transfer for atom transfer radical polymerization method (ARGET ATRP). The preparation technique for magnetic CTPEs opened a new route toward developing a wide spectrum of magnetic elastomeric materials with strongly enhanced macroscopic properties. Differential scanning calorimetry (DSC) was used to measure the glass transition temperatures, and thermogravimetric analysis (TGA) was used to examine thermal stabilities of these CTPEs. The magnetic property could be conveniently tuned by adjusting the content of Fe_3O_4 nanoparticles in CTPEs. Compared to their linear copolymers, these magnetic CTPEs showed significant increases in tensile strength and elastic recovery. In situ small-angle X-ray scattering measurement was conducted to reveal the microstructural evolution of CTPEs during tensile deformation.

KEYWORDS: *cross-linking, network, glass transition temperature, magnetite, ARGET ATRP*

INTRODUCTION

Polymer composites filled with natural or synthetic minerals have attracted increasing attention because the physical properties of the composites can be significantly different from those of the corresponding bulk polymers.[1,2] In general, the properties of polymer composites largely depend on the dispersion state of the reinforcing nanoparticles.[3] Macroscopic reinforcing elements always contain imperfections and there are no or weak interactions between the fillers and polymer matrix in the resulting composites. Smaller reinforcing elements have better structural perfection, but they tend to aggregate rather than disperse homogeneously in polymer matrix due to their large external surface areas.[4] Therefore, the surface of nanoparticles, interfacial areas, and polymer matrix have to be considered when designing composites with desired superior properties. In the past decade, magnetic iron oxide nanoparticles, especially magnetite (Fe_3O_4) and maghemite (γ-Fe_2O_3), have attracted tremendous attention because of their high magnetization, low toxicities, and fascinating applications in magnetic resonance imaging contrast enhancement,[5,6] site-specific drug delivery,[7,8] tissue engineering,[9] biological fluids,[10] cell separation,[11,12] and so on. The doping of polymers with inorganic magnetic nanoparticles appeared to be an appealing and robust method to produce highly efficient magnetic-responsive materials, and these small magnets in the resulting composites allowed them to respond to weak stimuli with a significant effect by alternating magnetic field.[13] A newly developed class of morphing materials called magnet filler–polymer matrix composites, which combine the functionality of a highly elastic polymer matrix with the driving force produced by the action of external magnetic fields on the magnetic fillers, has received great interest.[14]

Received: March 12, 2015
Accepted: April 30, 2015
Published: May 8, 2015

ACS Publications © 2015 American Chemical Society

DOI: 10.1021/acsami.5b02208
ACS Appl. Mater. Interfaces 2015, 7, 10563−10575

Scheme 1. Illustration of Syntheses of the Initiator-Functionalized Fe_3O_4 Nanoparticles (Fe_3O_4–BiB) and Magnetic Composite Thermoplastic Elastomer [Fe_3O_4-*g*-P(BA-*co*-MMA)]

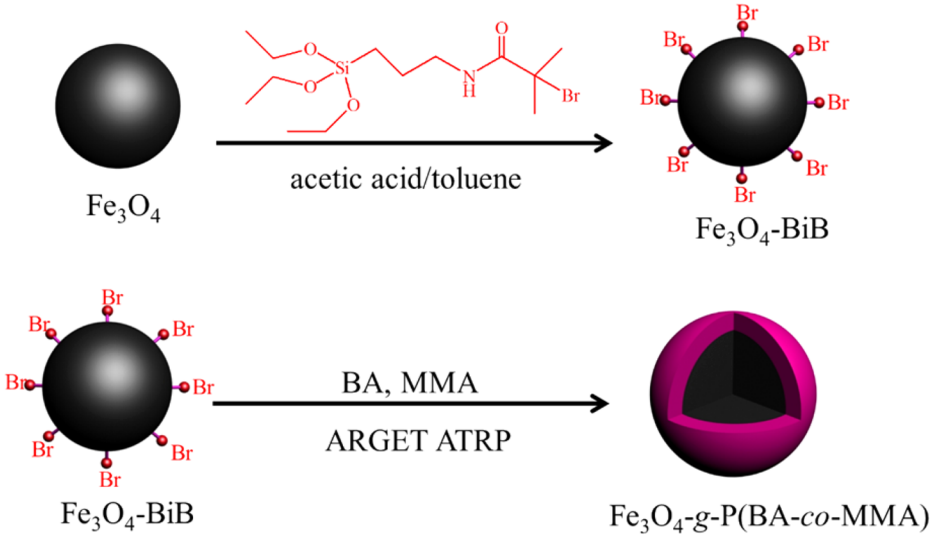

Elastomeric polymer materials are widely used for a myriad of important applications in our daily life, like automotive parts, adhesives, household goods, clothing, electronics, sporting goods, and medical devices.[15−18] In general, nonreinforced polymer matrixes are soft and fragile; thus, they do not exhibit suitable mechanical properties for practical applications. Interestingly, incorporation of semirigid cellulose chains or multiwalled carbon nanotubes into the elastomeric polymer matrixes via the grafting methods can dramatically improve the mechanical properties of composite thermoplastic elastomers (CTPEs).[19,20] On the other hand, combining the elastic and magnetic properties enables the resulting elastomeric composites to respond to external magnetic fields and leads to various striking phenomena. These flexible magnetic composites, known as magnetic elastomers, have been successfully used as magnetic cores and permanent magnets, connecting and fixing elements in various areas.[21] Considerable flexibility is desired in the choice of polymeric matrix for designing magnetic elastomeric composites. Polyurethanes,[22] natural or synthetic rubber,[23] and silicone elastomers[24] are commonly used elastomeric polymer matrixes. It has been well-accepted that filling of nanoparticles into polymer matrixes can result in materials with significantly improved properties.[25] However, a sufficiently homogeneous dispersion state of the nanoparticles is crucial for optimizing desired properties for these elastomeric composites. There are numerous strategies to control the nanoparticle dispersion in a polymer matrix. Suspending magnetic nanoparticles grafted with polymer chains in a polymer matrix seems to be an easy and efficient method. Thus, surface-initiated controlled polymerization approaches have been applied using atom transfer radical polymerization (ATRP) to polymerize various monomers from magnetic nanoparticles with immobilized initiators.[26−29] In fact, the ATRP method shows a high tolerance toward functional groups, resulting in polymers with narrow molecular mass distributions and defined end groups. García et al. demonstrated that magnetic Fe_3O_4 nanoparticles modified with polystyrene (PS) brushes could be selectively dispersed within the PS domains in a microphase-separated elastomeric matrix, polystyrene-*b*-polybutadiene-*b*-polystyrene (SBS) triblock copolymer.[4,30] The modified Fe_3O_4 nanoparticles showed improved dispersion and affinity for the PS domains. Besides serving as a scaffold to organize the magnetic nanoparticles, the thermoplastic elastomer SBS acted as a structural component to control interparticle distances and provide the mechanical integrity.

In this work, we made our efforts to synthesize magnetic composite thermoplastic elastomers (CTPEs) in which poly(*n*-butyl acrylate-*co*-methyl methacrylate) [P(BA-*co*-MMA)] copolymers were grafted from superparamagnetic Fe_3O_4 nanoparticles via activators regenerated by electron transfer for atom transfer radical polymerization (ARGET ATRP), as illustrated in Scheme 1. As one of the most robust and powerful techniques ARGET ATRP has been widely applied to prepare well-defined polymeric materials with complex architectures, and the significantly low concentration of catalysts used in polymerization is commercially and environmentally beneficial.[31−34] By manipulating the composition of the grafted rubbery matrix and the content of Fe_3O_4 nanoparticles, a broad spectrum of magnetic CTPEs with varied thermal, mechanical, and magnetic properties could be obtained. The as-prepared CTPEs could be easily fabricated via solvent casting. This versatile, one-pot approach can be further applied to develop other magnetic elastomers with superior properties. To the best of our knowledge, there has been little research to report on the preparation of magnetic thermoplastic elastomers via the ARGET ATRP method.

EXPERIMENTAL SECTION

Materials. Iron(III) chloride hexahydrate ($FeCl_3{\cdot}6H_2O$), sodium acetate (NaOAc) (anhydrous), ethylene glycol, γ-aminopropyl triethoxysilane, triethylamine (TEA), *n*-butyl acrylate (BA), methyl methacrylate (MMA), *N*,*N*-dimethylformamide (DMF), toluene, $Cu^{II}Br_2$, and copper wire (diameter 0.5 mm) were purchased from Sinopharm Chemical Reagent Co. (Shanghai, China). Analytical-grade ethyl 2-bromoisobutyrate (EBiB, 98%), 2-bromoisobutyryl bromide (98%), and polyethylene glycol (PEG) were purchased from Aldrich. *N*,*N*,*N*′,*N*″,*N*″-Pentamethyldiethylenetriamine (PMDETA, 98%) was purchased from TCI. MMA and BA were distilled under vacuum and DMF and toluene were distilled and kept in the presence of 4 Å molecular sieve prior to use. All other reagents were used as received.

Synthesis of Fe_3O_4 Nanoparticles. Fe_3O_4 nanoparticles were synthesized in a hydrothermal system according to the literature.[35]

DOI: 10.1021/acsami.5b02208
ACS Appl. Mater. Interfaces 2015, 7, 10563−10575

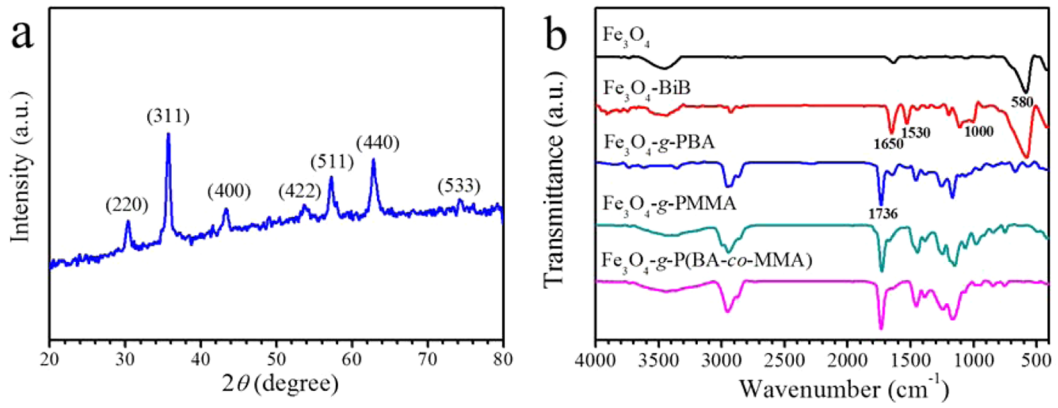

Figure 1. (a) XRD pattern of as-prepared Fe_3O_4 nanoparticles. (b) FTIR spectra of Fe_3O_4 nanoparticles, initiator-functionalized Fe_3O_4 nanoparticles (Fe_3O_4—BiB), Fe_3O_4-*g*-PBA, Fe_3O_4-*g*-PMMA, and Fe_3O_4-*g*-P(BA-*co*-MMA) (sample code BA6000-$Fe_3O_4$1.3).

Briefly, $FeCl_3{\cdot}6H_2O$ (6.75 g, 25 mmol) was dissolved in ethylene glycol (200 mL) to form a clear solution, and then NaOAc (18.0 g) and PEG (5 g) were added in. The mixture was stirred vigorously for 30 min and then sealed in a Teflon-lined stainless steel autoclave (250 mL capacity). After being heated to and maintained at 200 °C for 8 h, the autoclave was allowed to cool to room temperature. The obtained black product was washed five times with ethanol and then dried under vacuum at 60 °C until constant mass.

Preparation of Initiator-Functionalized Fe_3O_4 Nanoparticles (Fe_3O_4—BiB). The ATRP initiator was synthesized via the reaction of 2-bromoisobutyryl bromide and γ-aminopropyl triethoxysilane as previously reported.[36,37] Typically, γ-aminopropyl triethoxysilane (9.4 mL, 50 mmol) and TEA (7.0 mL, 50 mmol) were dissolved in toluene (50 mL), and then 2-bromoisobutyryl bromide (6.4 mL, 50 mmol) was added dropwise to the above solution at 0 °C. With an initial reaction at 0 °C for 3 h, a continuous overnight reaction was allowed in the mixture at room temperature, and then the mixture was filtered to remove the salts. The solvent and unreacted TEA were removed from the filtrate by evaporation under reduced pressure. For synthesis of Fe_3O_4—BiB, Fe_3O_4 nanoparticles (1.0 g) were added in toluene (200 mL) mixed with acetic acid (0.5 mL), and then the ATRP initiator (3.2 g, 8.6 mmol) was added in. Under the protection of argon, the mixture was stirred at room temperature for 72 h. The resulted product was precipitated in ethanol and then washed with ethanol five times to remove the excess initiator. The product was collected and dried under vacuum at 40 °C. Elemental analysis of Fe_3O_4—BiB revealed a composition of 4.3% carbon, 1.4% hydrogen, and 1.4% bromine, which indicated that there was about 0.18 mmol of initiator groups per gram of Fe_3O_4—BiB.

Synthesis of Fe_3O_4-*g*-P(BA-*co*-MMA). A typical graft copolymerization to prepare Fe_3O_4-*g*-P(BA-*co*-MMA) is described as follows: Fe_3O_4—BiB (111.2 mg, 0.02 mmol of Br) was dispersed in DMF (20 mL) in a flask, and then the catalyst $Cu^{II}Br_2$ (0.4 mg, 0.002 mmol) and ligand PMDETA (0.7 mg, 0.004 mmol) were added in. Subsequently, BA (15.4 g, 120 mmol), MMA (8.0 g, 80 mmol), and a copper wire (20 cm in length) were introduced into the flask. After being degassed by three freeze—pump—thaw cycles, the flask was sealed and the copolymerization was allowed to occur at 70 °C with stirring. With the intention to stop the copolymerization, the flask was opened and the resulted product was poured into excessive cold methanol, and the precipitate was washed and dried under vacuum at 40 °C until a constant mass. Copolymerizations of BA and MMA on Fe_3O_4—BiB were performed at different monomer feed ratios in this work. With ethyl 2-bromoisobutyrate (EBiB) as the initiator, linear P(BA-*co*-MMA) copolymers were synthesized via ARGET ATRP by following the same procedure as in our previous work.[18] The film samples with thicknesses of 0.3—0.6 mm were obtained by casting DMF solutions of 10 wt % Fe_3O_4-*g*-P(BA-*co*-MMA) in Teflon molds followed by removal of the solvent at 50 °C for 48 h. The films were further dried under vacuum at 80 °C until constant masses.

Cleavage of Grafted P(BA-*co*-MMA) from Fe_3O_4-*g*-P(BA-*co*-MMA). The typical cleavage procedure is described as follows: Fe_3O_4-*g*-P(BA-*co*-MMA) (100 mg) was dispersed in DMF (10 mL), and then 32% HCl solution (2 mL) was added in. The mixture was stirred overnight and the cleaved P(BA-*co*-MMA) copolymer was washed five times with methanol and then dried under vacuum at 40 °C until a constant mass.

Characterization and Measurements. Various advanced technologies were employed to characterize and measure the chemical structures, molecular masses, molecular mass distributions, thermal stabilities, glass transition temperatures, phase morphologies, and mechanical properties of Fe_3O_4-*g*-P(BA-*co*-MMA) and the related samples. The detailed experimental descriptions about these technologies have been provided in our previous work,[17—19] including Fourier transform infrared spectroscopy (FTIR), nuclear magnetic resonance spectroscopy (NMR), gel permeation chromatography (GPC), thermogravimetric analysis (TGA), differential scanning calorimetry (DSC), transmission electron microscopy (TEM), small-angle X-ray scattering (SAXS), and mechanical tensile property tests. Additional two technologies specifically employed in this work were X-ray diffraction (XRD) and magnetic property measurements. The X-ray diffraction was measured in a 2θ range from 20° to 80° with Cu Kα radiation on a TTR-III high-power X-ray powder diffractometer, and the measurements of magnetization curves were carried out using a superconducting quantum interference device (SQUID) at 300 K.

RESULTS AND DISCUSSION

Synthesis of Fe_3O_4-*g*-P(BA-*co*-MMA). The Fe_3O_4 nanoparticles were prepared via a hydrothermal method[35] and were further functionalized with ATRP initiator through the condensation of silanol groups.[36,37] Then, ARGET ATRP was chosen as the grafting-from strategy to synthesize Fe_3O_4-*g*-P(BA-*co*-MMA). XRD was used to determine the crystallographic structure of Fe_3O_4 nanoparticles. The XRD intensity profile of as-prepared Fe_3O_4 nanoparticles (Figure 1a) shows the major diffraction peaks corresponding to Fe_3O_4 nanoparticles. The 2θ values of 30.2°, 35.7°, 43.3°, 53.7°, 57.2°, 62.8°, and 74.3° are attributed to the (220), (311), (400), (422), (511), (440), and (533) planes of Fe_3O_4, respectively.[38] The FTIR spectra of Fe_3O_4 nanoparticles, initiator-functionalized Fe_3O_4 nanoparticles, Fe_3O_4-*g*-PBA, Fe_3O_4-*g*-PMMA, and Fe_3O_4-*g*-P(BA-*co*-MMA) are shown in Figure 1b. A characteristic absorption band relating to the Fe—O vibration at around 580 cm^{-1} can be seen in the spectrum of Fe_3O_4 nanoparticles. After being functionalized with the ATRP initiator, the absorption bands at 1650 and 1530 cm^{-1} for the N—C═O bond and at around 1000 cm^{-1} for the Si—O—Si vibration can be clearly seen, indicating the silanization of Fe_3O_4 nano-

DOI: 10.1021/acsami.5b02208
ACS Appl. Mater. Interfaces 2015, 7, 10563—10575

Table 1. Synthetic Formulae and Characteristics of Fe_3O_4-*g*-P(BA-*co*-MMA)

sample code[a]	molar ratio[b]	Fe_3O_4 content (wt %)	MMA content[c] (wt %)	M_n (grafts)[d] (kg/mol)	M_w/M_n[d]	T_g[e] (°C)
BA10000-$Fe_3O_4$1.2	1/10000/0/−/0.1/0.2	1.2	0	486	1.4	−46
BA7000-$Fe_3O_4$1.3	1/7000/3000/−/0.1/0.2	1.3	41.6	476	1.4	4
BA6500-$Fe_3O_4$0.8	1/6500/3500/−/0.1/0.2	0.8	45.0	748	1.4	7
BA6500-$Fe_3O_4$1.4	1/6500/3500/−/0.1/0.2	1.4	47.1	447	1.5	12
BA6500-$Fe_3O_4$2.8	1/6500/3500/−/0.1/0.2	2.8	48.4	250	1.4	16
BA6500-$Fe_3O_4$4.9	1/6500/3500/−/0.1/0.2	4.9	49.3	149	1.5	19
BA6000-$Fe_3O_4$1.3	1/6000/4000/−/0.1/0.2	1.3	50.6	467	1.4	21
BA5500-$Fe_3O_4$1.3	1/5500/4500/−/0.1/0.2	1.3	56.1	459	1.4	28
BA0-$Fe_3O_4$1.3	1/0/10000/−/0.1/0.2	1.3	98.7	447	1.4	128

[a]Sample codes are labeled as follows: the numbers following "BA" represent the moles of BA and the numbers behind "Fe_3O_4" represent the mass percentage of Fe_3O_4. [b]Molar ratio: Fe_3O_4-BiB/BA/MMA/Cu^0/$Cu^{II}Br_2$/PMDETA. [c]Determined by ^{1}H NMR spectroscopy. [d]Determined by GPC. [e]Determined by DSC.

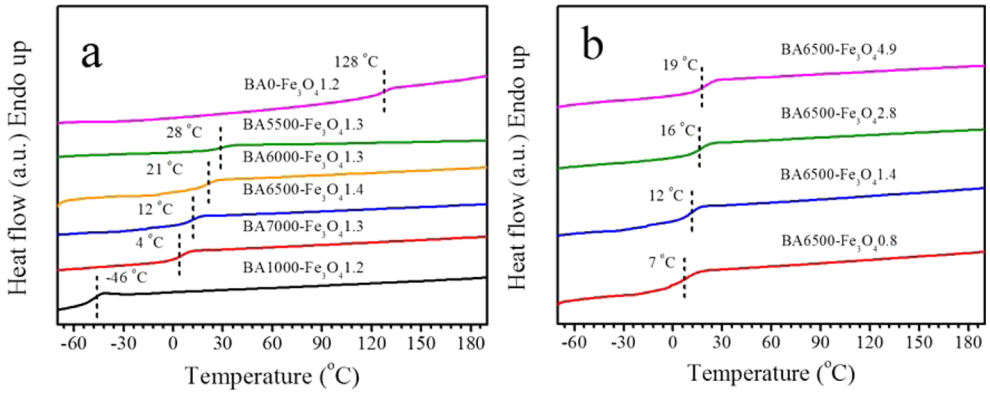

Figure 2. DSC heat flow curves under nitrogen atmosphere for (a) Fe_3O_4-*g*-P(BA-*co*-MMA) synthesized with varied monomer feed ratios and similar Fe_3O_4 contents and (b) Fe_3O_4-*g*-P(BA-*co*-MMA) synthesized with the same monomer feed ratio and varied Fe_3O_4 contents. A heating rate of 10 °C/min was applied. The dashed lines marked on the heat flow curves indicate the T_g.

particles.[36] After being grafted with PBA, PMMA, or P(BA-*co*-MMA) on the surface of Fe_3O_4 nanoparticles, the characteristic absorption bands at 1736 cm^{-1} for the C═O groups and at around 2900 cm^{-1} for the C−H stretching vibration can be seen, which attests to the successful grafting of polymer chains from Fe_3O_4 nanoparticles. The ^{1}H NMR spectrum of P(BA-*co*-MMA) copolymer cleaved from Fe_3O_4-*g*-P(BA-*co*-MMA) (sample code BA6000-$Fe_3O_4$1.3) is shown in Figure S1 (Supporting Information). A broad spectrum of magnetic CTPEs with varying glass transition temperatures can be fabricated by adjusting the composition of the grafted copolymers and the content of incorporated Fe_3O_4 nanoparticles (Table 1). Linear copolymer counterparts were synthesized for comparison purposes, with the details summarized in Table S1 (Supporting Information).

Thermal Properties of Fe_3O_4-*g*-P(BA-*co*-MMA). The glass transition temperatures (T_g) of the magnetic CTPEs were measured by using DSC. The DSC heat flow curves for Fe_3O_4-*g*-P(BA-*co*-MMA) and linear P(BA-*co*-MMA) copolymers are shown in Figures 2 and S2 (Supporting Information), respectively. All these DSC traces yielded singular T_g values. Obviously, the T_g values of the CTPEs can be controlled by manipulating the monomer feed ratio (MMA/BA), and the T_g values shift to higher values with increasing monomer feed ratio of MMA to BA, as exhibited in Figure 2a. At the same monomer feed ratio of MMA to BA, the T_g value increases from 7 to 19 °C with increasing Fe_3O_4 content, as shown in Figure 2b. The increase of T_g is a synergistic effect of MMA and Fe_3O_4 contents because the MMA content also increases with increasing Fe_3O_4 content. The increase of MMA and Fe_3O_4 contents in the graft copolymers lowers the flexibility of the chains, leading to higher T_g values. For such copolymer systems, the Fox equation can be used to investigate the correlation between T_g and the composition of the statistical copolymers[39,40]

$$\frac{1}{T_g} = \frac{w_1}{T_{g1}} + \frac{w_2}{T_{g2}} \quad (1)$$

where T_g is the glass transition temperature of the statistical copolymers, w_1 and w_2 are the mass contents of two repeat units in the copolymers, and T_{g1} and T_{g2} are the corresponding glass transition temperatures of the two homopolymers. The changes of T_g with MMA content for Fe_3O_4-*g*-P(BA-*co*-MMA) and linear P(BA-*co*-MMA) copolymers are shown in Figure S3 (Supporting Information) and demonstrate that the experimentally measured T_g values for both Fe_3O_4-*g*-P(BA-*co*-MMA) and linear P(BA-*co*-MMA) copolymers can be well-fitted by using the Fox equation, as indicated by the solid lines. This result strongly clarifies that the T_g values of Fe_3O_4-*g*-P(BA-*co*-MMA) can be well-controlled through the copolymerization process.

One of the most important limiting factors for applications of polymeric materials is their thermal stability. Figure 3 shows the TGA curves for Fe_3O_4 nanoparticles, Fe_3O_4−BiB, Fe_3O_4-*g*-PBA, Fe_3O_4-*g*-PMMA, and Fe_3O_4-*g*-P(BA-*co*-MMA). As the Fe_3O_4 nanoparticles remain almost stable in this temperature range, a small overall decline can be observed, which is caused by removal of residual surfactants. The initiator-functionalized

DOI: 10.1021/acsami.5b02208
ACS Appl. Mater. Interfaces 2015, 7, 10563−10575

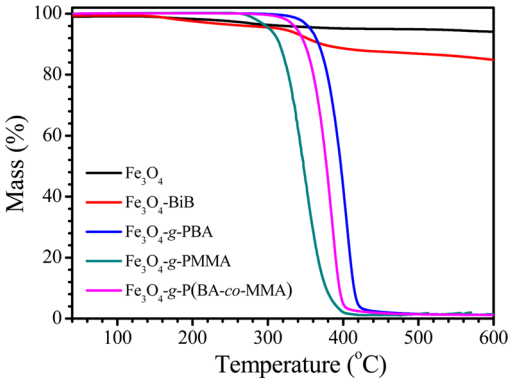

Figure 3. TGA curves measured under nitrogen atmosphere for Fe_3O_4 nanoparticles, Fe_3O_4–BiB, Fe_3O_4-*g*-PBA, Fe_3O_4-*g*-PMMA, and Fe_3O_4-*g*-P(BA-*co*-MMA) (sample code BA6000-$Fe_3O_4$1.3). The heating rate was 10 °C/min.

Fe_3O_4 nanoparticles give a two-stage decomposition profile, with the first stage of mass loss from 150 to 300 °C being due to the removal of residual ethylene glycol and PEG and the second stage from 300 to 450 °C being due to decomposition of the functional initiator. After grafting polymers from Fe_3O_4 nanoparticles, the TGA curves show a one-step thermal decomposition procedure, demonstrating successful graft polymerization. Fe_3O_4-*g*-PMMA shows the maximum decomposition at the temperature of 352 °C, whereas, Fe_3O_4-*g*-P(BA-*co*-MMA) and Fe_3O_4-*g*-PBA are much more stable, showing higher decomposition temperatures of 384 and 405 °C, respectively.

Phase Morphology of Fe_3O_4-*g*-P(BA-*co*-MMA). Most thermoplastic elastomers are essentially phase-separated systems, in which the rigid chain segments are dispersed as well-ordered minority phase domains in a matrix formed by the flexible polymer chains.[41,42] In the system of copolymer-grafted Fe_3O_4 nanoparticle composite thermoplastic elastomers, Fe_3O_4 nanoparticles and MMA glassy domains act as physical cross-linking points, which are well-dispersed in the soft PBA matrix, providing the enhanced mechanical properties. TEM images of Fe_3O_4 nanoparticles and sample BA6500-$Fe_3O_4$1.4 are shown in parts a and b of Figure 4, respectively. The Fe_3O_4 nanoparticle diameters are estimated to be about 100 nm, and the Fe_3O_4 nanoparticles are dispersed homogeneously in the bulk sample of BA6500-$Fe_3O_4$1.4. Figure 4c further shows the Lorentz-corrected small-angle X-ray scattering (SAXS) intensity profiles for Fe_3O_4-*g*-P(BA-*co*-MMA) synthesized with the same monomer feed ratio and varied Fe_3O_4 contents. The Lorentz correction can correct the differences in the time that the individual reciprocal lattice point spends on the surface of the Ewald sphere. It can be applied to scattering from the reciprocal lattices for which there is a periodicity with a large number of consecutive units in the systems. Because the Fe_3O_4 nanoparticles are randomly distributed in the copolymer matrix, the Lorentz correction [$I(q)$ multiplied by q^2] can be applied to investigate the phase morphology of the samples. It can be found that these Fe_3O_4-*g*-P(BA-*co*-MMA) samples show one strong correlation peak at the low q position and discernible weak secondary correlation peak at the high q position, depending on the Fe_3O_4 content. The strong SAXS correlation peak position (q_{max}) gradually shifts to higher values with increasing Fe_3O_4 content, as indicated by the dash line. Because the interparticle distance (d) can be estimated by using $d = 2\pi/$

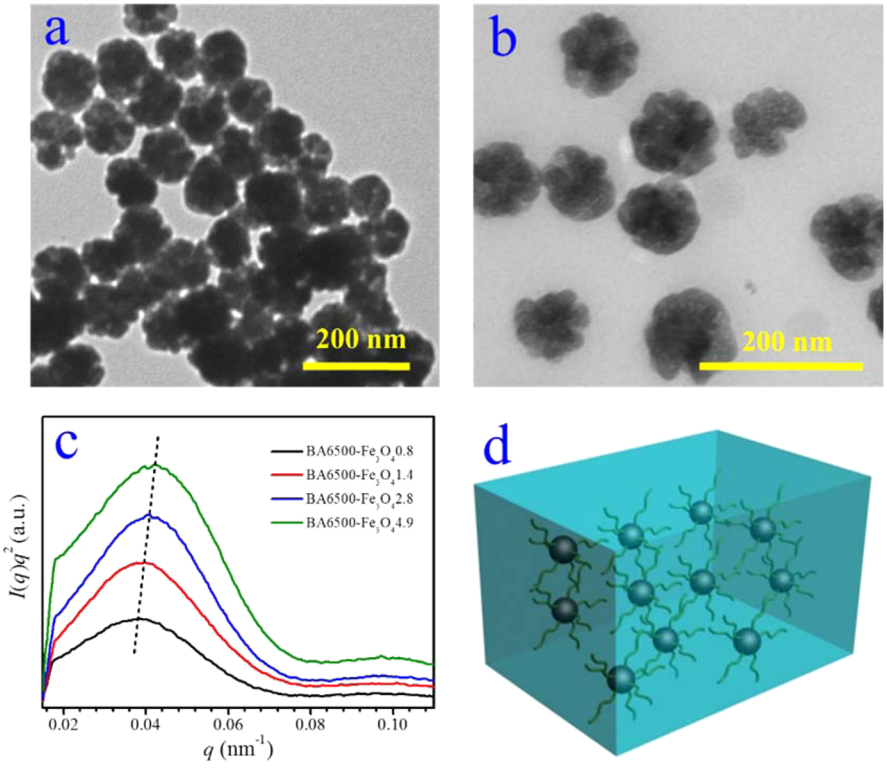

Figure 4. TEM images of (a) Fe_3O_4 nanoparticles and (b) sample BA6500-$Fe_3O_4$1.4. (c) Lorentz-corrected SAXS intensity profiles [$I(q)q^2$ versus q curves] for Fe_3O_4-*g*-P(BA-*co*-MMA) synthesized with the same monomer feed ratio and varied Fe_3O_4 contents. (d) Illustration of phase morphology for Fe_3O_4-*g*-P(BA-*co*-MMA).

DOI: 10.1021/acsami.5b02208
ACS Appl. Mater. Interfaces 2015, 7, 10563–10575

q_{max}, the result in Figure 4c indicates that the interparticle distance d decreases with increasing Fe_3O_4 content, which is obviously understandable. By considering the results measured from TEM and SAXS, the phase morphology of Fe_3O_4-*g*-P(BA-*co*-MMA) can be schematically illustrated in Figure 4d.

Magnetic Property of Fe_3O_4-*g*-P(BA-*co*-MMA). Figure 5a shows the magnetization curves in the applied magnetic field

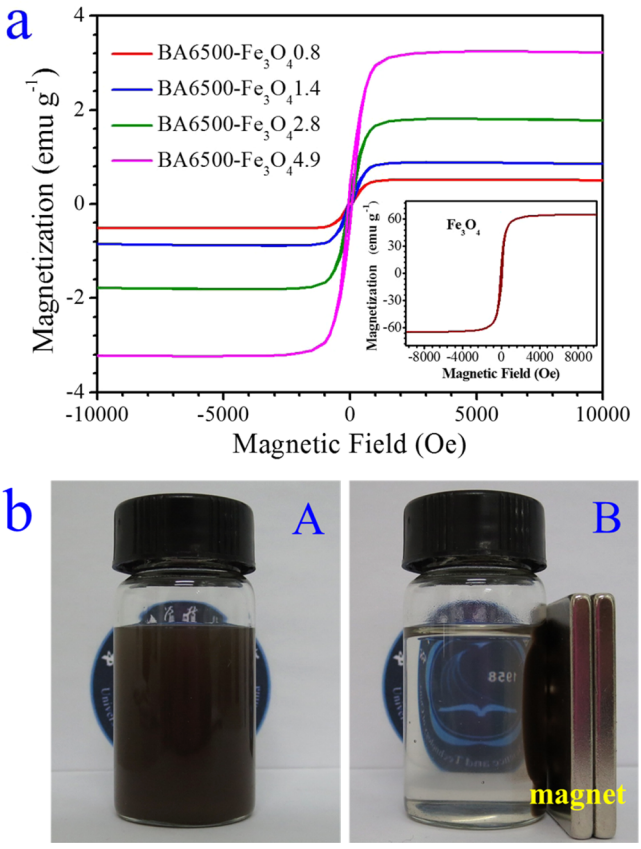

Figure 5. (a) Magnetization curves for BA6500-$Fe_3O_4$0.8, BA6500-$Fe_3O_4$1.4, BA6500-$Fe_3O_4$2.8, and BA6500-$Fe_3O_4$4.9 at room temperature. The inset shows the magnetization curve for Fe_3O_4 nanoparticles. (b) Photos of sample BA6500-$Fe_3O_4$1.4 in DMF (10 mg/mL) (A) prior to and (B) after exposure for 10 min to a permanent magnet.

at room temperature for as-prepared Fe_3O_4 nanoparticles and Fe_3O_4-*g*-P(BA-*co*-MMA) synthesized with the same monomer feed ratio and varied Fe_3O_4 contents. No remnant magnetization and coercivity are observed, revealing a superparamagnetic behavior for Fe_3O_4 nanoparticles.[37] The magnetic saturation value is 65.2 emu g^{-1} for Fe_3O_4 nanoparticles, and the magnetic saturation values are 0.5 emu g^{-1} for BA6500-$Fe_3O_4$0.8, 0.9 emu g^{-1} for BA6500-$Fe_3O_4$1.4, 1.8 emu g^{-1} for BA6500-$Fe_3O_4$2.8, and 3.2 emu g^{-1} for BA6500-$Fe_3O_4$4.9, illustrating that the magnetic saturation values of Fe_3O_4-*g*-P(BA-*co*-MMA) are proportional to the Fe_3O_4 content, which can be controlled by polymerization. Figure 5b shows the photos of sample BA6500-$Fe_3O_4$1.4 in DMF prior to and after exposure for 10 min to a permanent magnet. Sample BA6500-$Fe_3O_4$1.4 could be homogeneously dispersed in DMF to form a dark brown suspension. Whereas, when the suspension was put close to a permanent magnet, sample BA6500-$Fe_3O_4$1.4 was attracted to the magnet and the suspension became colorless, indicative of a magnetic interaction between sample BA6500-$Fe_3O_4$1.4 and the magnet.

Strongly Enhanced Mechanical Properties of Fe_3O_4-*g*-P(BA-*co*-MMA) CTPEs. Monotonic and step cyclic tensile tests were applied to investigate the mechanical properties of these copolymer-grafted Fe_3O_4 composite thermoplastic elastomers and their linear copolymer counterparts. The nominal stress−strain curves for Fe_3O_4-*g*-P(BA-*co*-MMA) CTPEs are displayed in Figure 6a,b, indicating the elastomeric behavior for these samples with the strain at break all above 450%. The monotonic nominal stress−strain curves for Fe_3O_4-*g*-P(BA-*co*-MMA) CTPEs with similar low Fe_3O_4 contents and their linear copolymer counterparts are compared in Figure S4 (Supporting Information), from which it can be obviously seen that the curves for Fe_3O_4-*g*-P(BA-*co*-MMA) are all above those for their corresponding linear copolymer counterparts, demonstrating significant enhancements of mechanical properties by introducing minute amounts of Fe_3O_4 nanoparticles as the stiff fillers in CTPEs. A strong strain-hardening behavior can be clearly seen for Fe_3O_4-*g*-P(BA-*co*-MMA) CTPEs, whereas the strain-hardening is much weaker for linear P(BA-*co*-MMA) copolymers. Tables 2 and S2 (Supporting Information) summarize the mechanical properties for Fe_3O_4-*g*-P(BA-*co*-MMA) CTPEs and their linear copolymer counterparts, respectively. The mechanical properties, including the stress and strain at break for linear PMMA-*b*-PBA-*b*-PMMA triblock or star PBA-*b*-PMMA block copolymers, had been investigated.[43−47] The 20-arm PBA-*b*-PMMA star block copolymer[47] showed the stress and strain at break of only 7.4 MPa and 375%, respectively, and linear PMMA-*b*-PBA-*b*-PMMA triblock copolymers[46] showed the stress and strain at break of only 4.2 MPa and 520%, respectively. However, Fe_3O_4-*g*-P(BA-*co*-MMA) CTPEs in this work show higher stress and strain at break (Table 2) than those triblock or star block copolymers.[43−47] In addition, the one-pot synthetic strategy for Fe_3O_4-*g*-P(BA-*co*-MMA) CTPEs is simple, which enhances the efficiency of the chemical reactions and avoids arduous separation and purification processes for the intermediate compounds.

According to Haward and Thackray,[48,49] the deformation in thermoplastics at large strains can be simplified to a model of a Hookean spring in series with a dashpot in parallel with another rubbery spring, which can describe all basic macroscopic effects that occur during tensile deformation.[50] In our case, the Hookean spring and the dashpot correspond to the hard phases, including glassy MMA chain segmental domains and the dispersed Fe_3O_4 nanoparticles, while the rubbery spring represents the amorphous PBA phase domains. In the Gaussian treatment, the true stress (σ_{true}) can be expressed by eq 2 as follows

$$\sigma_{true} = \lambda\sigma_{eng} = G_p(\lambda^2 - 1/\lambda) \quad (2)$$

where σ_{eng} is the engineering stress, λ the extension ratio, and G_p defined as the strain-hardening modulus. The true strain (ε_H) is related to λ by eq 3.

$$\varepsilon_H = \ln \lambda \quad (3)$$

Figure 6c,d shows the true stress−true strain curves for Fe_3O_4-*g*-P(BA-*co*-MMA) CTPEs, and the curve shapes indicate obvious strain-hardening at high strains. Figure 6e,f further shows the Gaussian plots of true stress as a function of $\lambda^2 - 1/\lambda$, from which the strain-hardening modulus (G_p) can be

DOI: 10.1021/acsami.5b02208
ACS Appl. Mater. Interfaces 2015, 7, 10563−10575

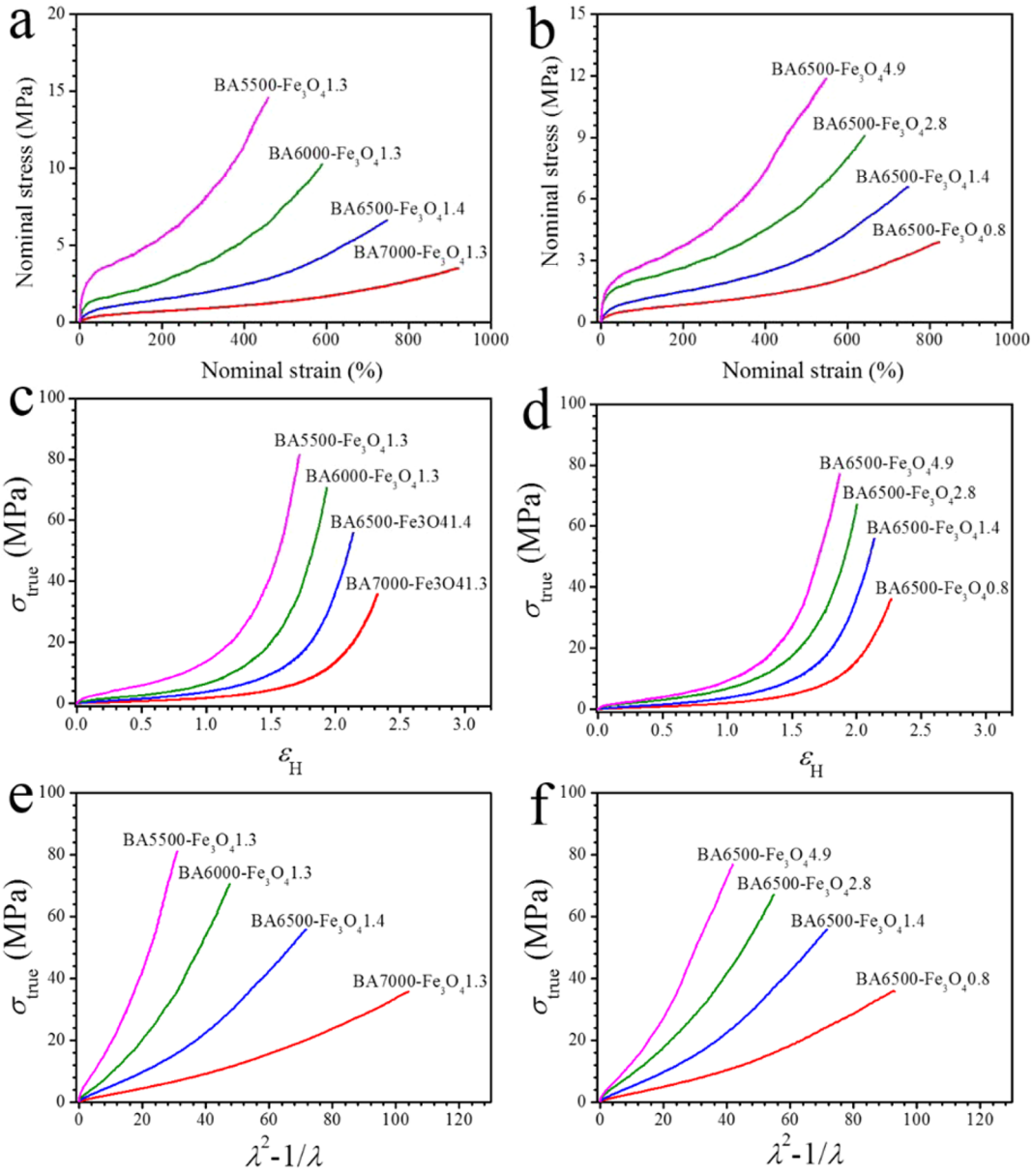

Figure 6. Monotonic nominal stress–strain curves (a, b), true stress–true strain curves (c, d), and the corresponding Gaussian plots (e, f) for Fe_3O_4-*g*-P(BA-*co*-MMA) CTPEs synthesized with varied monomer feed ratios and similar Fe_3O_4 contents (a, c, e) and the same monomer feed ratio and varied Fe_3O_4 contents (b, d, f).

Table 2. Mechanical Properties of Fe_3O_4-*g*-P(BA-*co*-MMA) CTPEs

	elastic recovery[a]				
sample code	at 225% strain (%)	average (%)	G_p[b] (MPa)	stress at break[c] (MPa)	strain at break[c] (%)
BA7000-$Fe_3O_4$1.3	99	95	0.3	3.5	921
BA6500-$Fe_3O_4$0.8	97	95	0.4	3.9	824
BA6500-$Fe_3O_4$1.4	98	94	0.7	6.6	747
BA6500-$Fe_3O_4$2.8	95	87	1.1	9.0	641
BA6500-$Fe_3O_4$4.9	91	80	1.7	11.9	548
BA6000-$Fe_3O_4$1.3	97	91	1.4	10.2	590
BA5500-$Fe_3O_4$1.3	68	57	2.4	14.6	458

[a]Determined from step cyclic nominal stress–strain curves. [b]Determined from the Gaussian plots. [c]Determined from monotonic nominal stress–strain curves.

obtained. The true stress–true strain curves and the corresponding Gaussian plots for linear P(BA-*co*-MMA) copolymers are shown in Figure S5 (Supporting Information). The strain-hardening modulus for linear P(BA-*co*-MMA) copolymers increases from 0.1 to 0.7 MPa with increasing MMA content (Table S2, Supporting Information), demonstrating that the value of G_p is related to the glassy MMA chain segmental domains. However, the increase of G_p is low. On the contrary, the increase of G_p is rather rapid for Fe_3O_4-*g*-P(BA-*co*-MMA) CTPEs, especially for the samples synthesized with the same monomer feed ratio. The G_p increases from 0.4 MPa (sample BA6500-$Fe_3O_4$0.8) to 1.7 MPa (sample BA6500-$Fe_3O_4$4.9) with increasing Fe_3O_4 content (Table 2). Meanwhile, the G_p values for Fe_3O_4-*g*-P(BA-*co*-MMA) CTPEs are larger than their linear copolymer counterparts, revealing that the incorporation of Fe_3O_4 nanoparticles strongly facilitates the strain-hardening behavior. Recently, Jancar et al. found that

DOI: 10.1021/acsami.5b02208
ACS Appl. Mater. Interfaces 2015, 7, 10563–10575

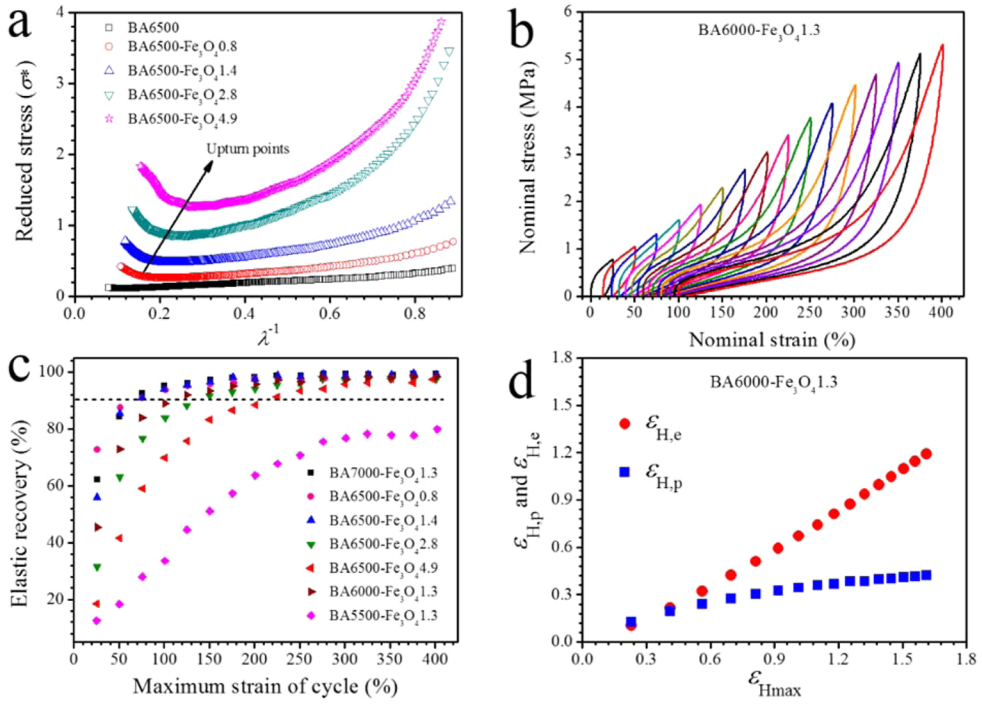

Figure 7. (a) Mooney–Rivlin plots for Fe_3O_4-*g*-P(BA-*co*-MMA) CTPEs synthesized with the same monomer feed ratio and varied Fe_3O_4 contents. (b) Nominal stress–strain curves for sample BA6000-$Fe_3O_4$1.3 during step cyclic tensile deformation with maximum strains of 25, 50, 75, 100, 125, 150, and so on up to 400%. (c) Changes of elastic recovery with maximum strain in each cyclic step for Fe_3O_4-*g*-P(BA-*co*-MMA) CTPEs. The elastic recovery value of 90% is indicated by the short dashed line. (d) Changes of true plastic strain ($\varepsilon_{H,p}$) and true elastic strain ($\varepsilon_{H,e}$) as functions of true maximal strain (ε_{Hmax}) for sample BA6000-$Fe_3O_4$1.3 during step cyclic deformation.

rigid spherical nanoparticles can increase the strain-hardening modulus of PMMA, with the enhancement being a function of nanoparticle content.[51] In our case, the P(BA-*co*-MMA) chains are immobilized on Fe_3O_4 nanoparticles due to chemical bonding between the nanoparticle fillers and polymer matrix. Thus, the strain-hardening behavior can be sustained by Fe_3O_4 nanoparticles.

The elastomeric network and interfacial interaction in CTPEs can be evaluated by using the well-known Mooney–Rivlin equation (eq 4) as follows[52]

$$\sigma^* = \sigma_{eng}/(\lambda - \lambda^{-2}) = 2C_1 + 2C_2\lambda^{-1} \quad (4)$$

where σ^* is the reduced stress and $2C_1$ and $2C_2$ are constants that are independent of λ. The changes of reduced stress σ^* with the reciprocal of extension ratio (λ^{-1}) for Fe_3O_4-*g*-P(BA-*co*-MMA) CTPEs synthesized with the same monomer feed ratio and varied Fe_3O_4 contents are illustrated in Figure 7a. The reduced stress for BA6500 (with no Fe_3O_4 nanoparticles) only shows a slight change, whereas the reduced stress for Fe_3O_4-*g*-P(BA-*co*-MMA) CTPEs shows an obvious abrupt upturn at high deformations. This upturn is attributed to the limited chain extensibility of polymer chains bridging the neighboring Fe_3O_4 nanoparticles during tensile deformation. Moreover, as the content of Fe_3O_4 nanoparticles increases, both the absolute value of reduced stress and the value of λ^{-1} at which the upturn point appears increase gradually, indicating that Fe_3O_4 nanoparticles can serve as physical cross-linking points in such type of CTPEs. The improved dispersion of Fe_3O_4 nanoparticles and interfacial interactions between nanoparticles and copolymer chains through chemical bonding (graft polymerization) can promote polymer chain orientation among adjacent cross-linking points during tensile deformation because the copolymer chains are anchored on the nanoparticles.

Figure 7b shows typical nominal stress–strain curves for sample BA6000-$Fe_3O_4$1.3 during step cyclic deformation with maximum strains of 25, 50, 75, 100, 125, 150, and so on up to 400%. It can be found that the ascending curve in a given cycle follows a quite different path from that of the descending curve in the previous cycle. With several cycles, the ascending curve becomes concave-upward, and the residual strains at zero stress become progressively larger due to plastic deformation, also known as stress-softening. Nominal stress–strain curves for other Fe_3O_4-*g*-P(BA-*co*-MMA) CTPEs and their linear copolymer counterparts are shown in Figures S6 and S7 (Supporting Information). The stress-softening and hysteresis for Fe_3O_4-*g*-P(BA-*co*-MMA) CTPEs are due to the Mullins effect, which is often found in nanoparticle-filled elastomers and semicrystalline polyolefin-based block copolymers.[53,54] For thermoplastic elastomers, elasticity is the ability to return to their initial state once the applied force is removed. The elastic recovery (ER) can be calculated from the nominal stress–strain curves as ER = 100% × $[\varepsilon_{max} - \varepsilon(0,\varepsilon_{max})]/\varepsilon_{max}$, where ε_{max} and $\varepsilon(0,\varepsilon_{max})$ are the maximum strain in the cycle and the strain at zero stress after the maximum strain ε_{max}, respectively. The changes of elastic recovery with maximum strain in each cyclic step for Fe_3O_4-*g*-P(BA-*co*-MMA) CTPEs and their linear copolymer counterparts during cyclic tensile deformation are shown in Figures 7c and S8 (Supporting Information), respectively. Elastic recovery can be significantly increased after several loading–unloading cycles. Moreover, the plateau regions of elastic recovery appear at higher strains, and the strain for reaching the plateau region increases with increasing MMA content. Bazan and co-workers recently synthesized elastomers by grafting BA from polyethylene copolymer

DOI: 10.1021/acsami.5b02208
ACS Appl. Mater. Interfaces 2015, 7, 10563–10575

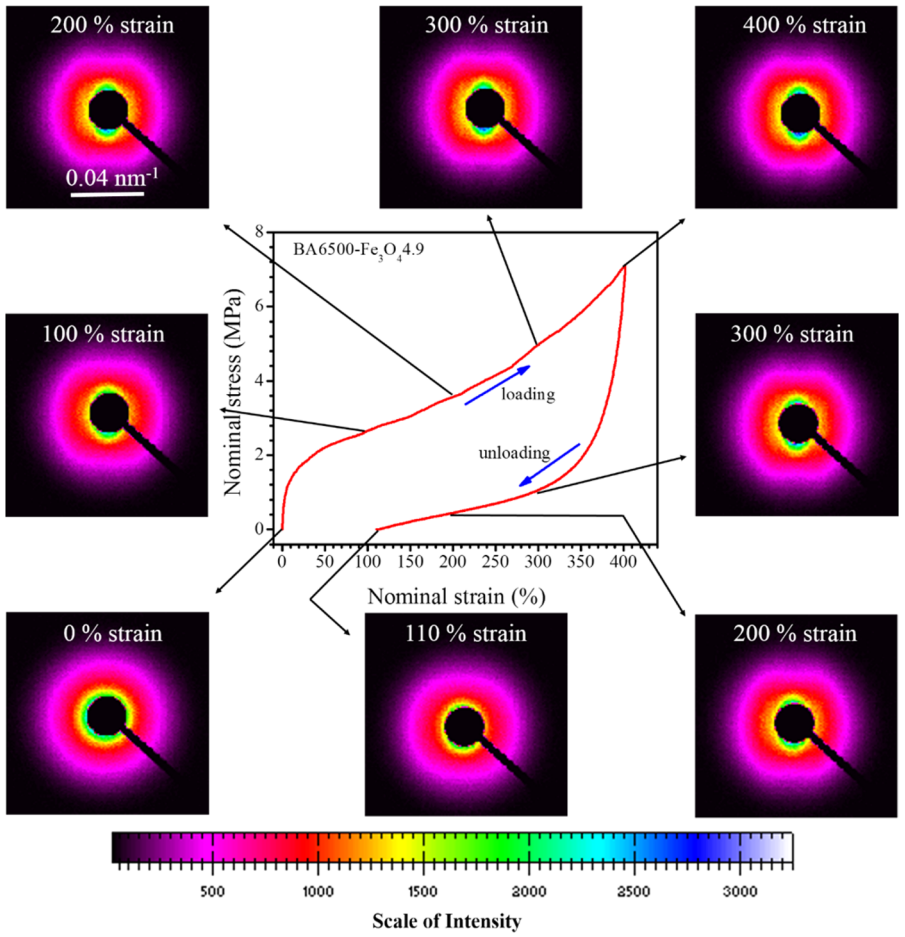

Figure 8. Nominal stress–strain curve and typical SAXS patterns during extension (loading) and retraction (unloading) of sample BA6500-$Fe_3O_4$4.9. Each SAXS pattern was taken at the strain indicated by the arrows. The stretching direction is horizontal.

macroinitiator, and their elastomers showed high-performance mechanical properties.[55,56] In their work, the grafting process rendered the new elastic materials significantly softer and more elastic, and the best-performing material exhibited an average elastic recovery of 86%.[55] However, the ER values of their synthesized materials decrease as the maximum strain in the cycles increases. In our case, the ER values of Fe_3O_4-*g*-P(BA-*co*-MMA) CTPEs (except for sample BA5500-$Fe_3O_4$1.3) during step cyclic tensile deformation are all above 90% at a strain of 225%. During the step cyclic test, a stepwise stretching of the specimen with a certain strain rate was interrupted after each step with an unloading–loading cycle, leading to a splitting of the total true strain (ε_H) into an unrecoverable true plastic strain ($\varepsilon_{H,p}$) (remaining strain at zero stress) and a recoverable true elastic strain ($\varepsilon_{H,e}$) (recovered strain after unloading), and the true maximal strain of the cycle N is called ε_{Hmax}.[15,57] Figure 7d shows the changes of true elastic strain and plastic strain with true maximum strain of each cycle for sample BA6000-$Fe_3O_4$1.3 during step cyclic tensile deformation. The true elastic strain is low at first, and then it increases rapidly with increasing true maximum strain. However, the true plastic strain slightly increases with the increase of the true maximum strain in each cycle. After several loading–unloading cycles, the true elastic strain becomes much higher than the true plastic strain, indicating the sufficient elasticity of this sample. The evolution of the true plastic and elastic strain as a function of the true maximum strain of each cycle for other Fe_3O_4-*g*-P(BA-*co*-MMA) CTPEs and their linear copolymer counterparts is shown in Figures S9 and S10 (Supporting Information), respectively. Note that the true elastic strain is always lower than the true plastic strain for sample BA6000 (Figure S10c, Supporting Information), which is quite different from the trend for sample BA6000-$Fe_3O_4$1.3, indicating the strong enhancement of elasticity for copolymer-grafted CTPEs by incorporation of Fe_3O_4 nanoparticles as multiple physical cross-linking points. In the case of elastomers, the major effect of loading is to stretch the network chains, substantially reducing the entropy, and a retractive force arises primarily due to the tendency for the system to increase the reduced entropy toward the maximum value it has stored in the undeformed state.[58] Because P(BA-*co*-MMA) copolymer chains are immobilized onto Fe_3O_4 nanoparticles, it is difficult to stretch out the copolymer chains and break the networks, leading to high-performance elastic properties.

Structural Evolutions of Fe_3O_4-*g*-P(BA-*co*-MMA) CTPEs during Tensile Deformation. Observations of tensile deformation of thermoplastic elastomers are important to understand the fundamental behavior in a controlled system. Therefore, it is essential to investigate the morphological development for copolymer-grafted Fe_3O_4 composite thermoplastic elastomers under uniaxial deformation. Ezquerra and his co-workers have found that the deformation mechanisms of various nanocomposite elastomers can be investigated "in situ" by combining small- and wide-angle X-ray scattering techniques

DOI: 10.1021/acsami.5b02208
ACS Appl. Mater. Interfaces 2015, 7, 10563–10575

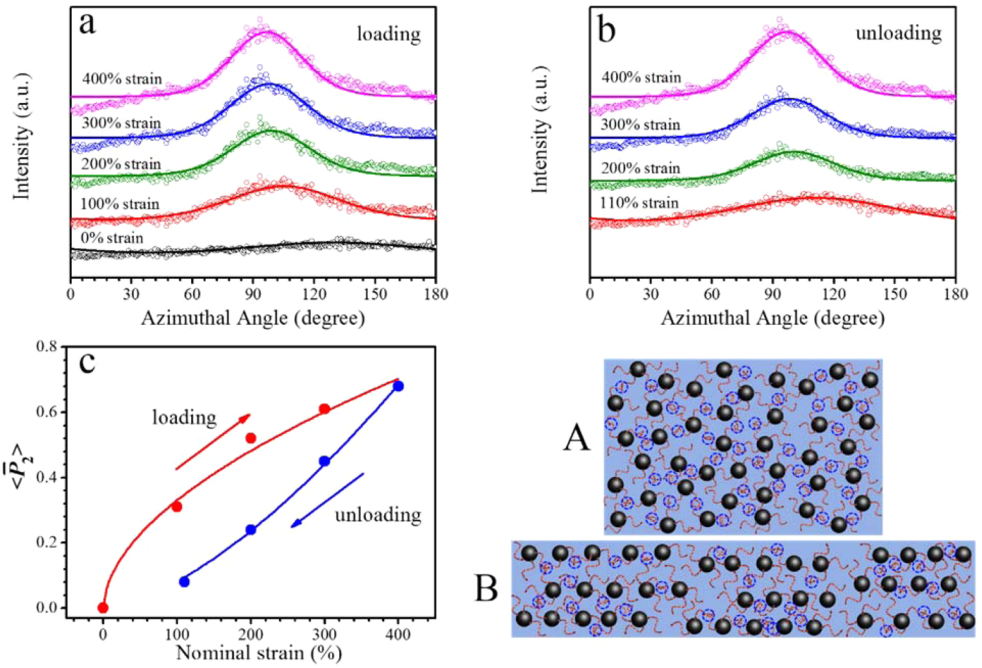

Figure 9. Azimuthal scattering intensity profiles at different strains for sample BA6500-$Fe_3O_4$4.9 during (a) loading and (b) unloading processes. Change of orientational order parameter, $\langle \overline{P}_2 \rangle$, with strain for Fe_3O_4 nanoparticles in sample BA6500-$Fe_3O_4$4.9 during loading and unloading processes (c). The arrows indicate the loading and unloading processes, respectively. The solid lines are guide for the eyes. Schematic illustrations of unaligned (cartoon A) and aligned (cartoon B) Fe_3O_4 nanoparticles in CTPEs before and during tensile deformation, respectively. The stretching direction is horizontal. The black spheres represent Fe_3O_4 nanoparticles, and phase domains in blue circles represent the physical cross-linking points due to aggregation of MMA chain segments.

(SAXS and WAXS) with the stress−strain experiments in a simultaneous fashion.[59−62] In order to elucidate the microstructural changes of the magnetic CTPEs in detail, in situ SAXS measurements were performed during extension (loading) and subsequent retraction (unloading) processes. The nominal stress−strain curve and typical SAXS patterns taken during extension (loading) and retraction (unloading) for a typical sample BA6500-$Fe_3O_4$4.9 are shown in Figure 8. The arrows indicate the strain values where the SAXS patterns were taken. The nominal stress−strain curve shows a hysteresis during loading and unloading processes, and the lack of a complete recovery is due to the plastic deformation during tensile deformation. Before tensile deformation (0% strain), the two-dimensional SAXS pattern demonstrates an isotropic phase, indicating that Fe_3O_4 nanoparticles are randomly distributed throughout the sample. During the loading process, a typical anisotropic scattering pattern (100% strain) is observed, indicating that the copolymer-grafted Fe_3O_4 nanoparticles are forced to be orientated along the stretching direction. Moreover, the SAXS patterns become more anisotropic as the strain increases. During the unloading process, the SAXS patterns gradually approach that at the initial state as the strain decreases, but they do not completely recover due to the plastic deformation. It should be noted that linear P(BA-*co*-MMA) copolymers do not show any detectable SAXS patterns during loading or unloading process due to the absence of an electronic density contrast in these samples.

The azimuthal scattering intensity profiles for sample BA6500-$Fe_3O_4$4.9 at different strains during loading and unloading processes can be extracted from the SAXS patterns by integration at a scattering vector of q = 0.015 nm^{-1} after subtracting the air scattering intensity, and the results are shown in Figure 9a,b. The azimuthal scattering intensity profile does not show any obvious peak at 0% strain, demonstrating that the Fe_3O_4 nanoparticles are randomly dispersed in the sample before loading. However, peaks appear in the azimuthal scattering intensity profiles at $\phi \approx 90°$ (Figure 9a) and 270° (not shown in Figure 9a) when sample BA6500-$Fe_3O_4$4.9 was stretched to 100% strain, which means that the Fe_3O_4 nanoparticles are aligned along the tensile direction. The azimuthal scattering intensity peaks become narrower with increasing strain during loading, illustrating that the orientation of Fe_3O_4 nanoparticles is strongly related to the strain. In order to clarify, the azimuthal scattering intensity profile is fitted by the Maier−Saupe distribution function as follows[63]

$$I = I_0 + A \exp[\beta \cos^2(\phi - \phi_0)] \tag{5}$$

where I_0 is the baseline intensity, β is a parameter that determines the width of distribution, ϕ is the azimuthal angle, and ϕ_0 is the azimuthal angle at the position with the maximal intensity. The fitted results are shown in Figure 9a,b as the solid lines, from which β can be obtained. Then the orientational order parameter ($\langle \overline{P}_2 \rangle$) ranging between 0 and 1 can be calculated as follows[64]

$$\langle \overline{P}_2 \rangle = \frac{\int_{-1}^{1} P_2(\cos\phi) \exp(\beta \cos^2\phi)\, d(\cos\phi)}{\int_{-1}^{1} \exp(\beta \cos^2\phi)\, d(\cos\phi)} \tag{6}$$

where the function $P_2(\cos\phi)$ is the second-order Legendre polynomial of cos ϕ, given by eq 7 as follows:

$$P_2(\cos\phi) = \frac{1}{2}(3\cos^2\phi - 1) \tag{7}$$

The changes of $\langle \overline{P}_2 \rangle$ for Fe_3O_4 nanoparticles with strain during loading and unloading processes are shown in Figure 9c.

DOI: 10.1021/acsami.5b02208
ACS Appl. Mater. Interfaces 2015, 7, 10563−10575

The value of $\langle \overline{P}_2 \rangle$ increases rapidly from 0 to 0.68 as the strain increases during loading, while the value of $\langle \overline{P}_2 \rangle$ decreases rapidly during the unloading process, indicating that the copolymer-grafted Fe_3O_4 nanoparticles are forced to be aligned along the tensile direction and $\langle \overline{P}_2 \rangle$ is strongly related to the strain of deformation. It should be noted that the values of $\langle \overline{P}_2 \rangle$ range between 0 and 1, with the former corresponding to an unaligned structure and the latter to perfect alignment along the director. The obtained value of $\langle \overline{P}_2 \rangle$ for sample BA6500-$Fe_3O_4$4.9 at the strain of 400% is 0.68, indicating that Fe_3O_4 nanoparticles are well-aligned in the elastomeric matrix. However, during the unloading process, the aligned Fe_3O_4 nanoparticles cannot fully recover to their initial random distribution state after the stress release ($\langle \overline{P}_2 \rangle$ = 0.08) due to the occurrence of plastic deformation. The plastic deformation can be attributed to the slippage of the trapped entanglements in the copolymer matrix, and the slippage of copolymer chains is not instantaneously reversible, leading to the slight orientation of Fe_3O_4 nanoparticles after the stress release. It is necessary to clarify the structural evolution of CTPEs during extension and retraction. Before tensile deformation, Fe_3O_4 nanoparticles are randomly distributed in the copolymer matrix, as shown in cartoon A of Figure 9. When the sample is extended at low strains, the polymer chains between Fe_3O_4 nanoparticles and/or MMA chain segmental domains are stretched, which results in a decrease of entropy. At sufficiently high strains, both Fe_3O_4 nanoparticles and MMA chain segmental domains act as physical cross-linking points, leading to a rapid increase in stress. At the meanwhile, Fe_3O_4 nanoparticles are forced to become highly orientated along tensile direction, as illustrated in cartoon B of Figure 9, leading to an obvious strain-hardening behavior because the applied stress can be transferred to the orientated rigid Fe_3O_4 nanoparticles. During retraction, the stress and the orientation degree of Fe_3O_4 nanoparticles decrease quickly to recover the entropy of the nanoparticle-filled elastomeric copolymer system.

The ability to tailor the properties is required to develop nanocomposites for advanced technological applications. It should be noticed that the magnetism of copolymer-grafted Fe_3O_4 composite thermoplastic elastomers can be well-controlled by adjusting the content of Fe_3O_4 nanoparticles in CTPEs. In general, elastomeric polymer nanocomposites are prepared by dispersing nanoobjects into elastomeric polymer matrixes, and the actual reinforcing effects are strongly affected by the arrangement of the nanoobjects, which are often dispersed as fractal aggregates due to the surface activity of the fillers.[65] In our case, the copolymer chains in the rubbery matrix are grafted from the surface of Fe_3O_4 nanoparticles to prevent the aggregation of Fe_3O_4 nanoparticles, and the spacing between neighboring nanoparticles can be well-controlled. Thus, the copolymer-grafted Fe_3O_4 nanoparticles can be homogeneously distributed in the rubbery matrix, and the interfacial adhesion between nanoparticles and copolymer matrix becomes strong through chemical bonding. In such a way, Fe_3O_4 nanoparticles are introduced as physical cross-linking points, and the rubbery matrix can be interconnected by both Fe_3O_4 nanoparticles and glassy MMA chain segmental domains (cartoon A of Figure 9). Therefore, the applied stress during tensile deformation can be successfully transferred and sustained by Fe_3O_4 nanoparticles, leading to significantly enhanced modulus and stiffness, as well as higher elastic recovery, as compared with their linear copolymer counterparts.

CONCLUSIONS

In summary, we have designed and synthesized magnetic composite thermoplastic elastomers (CTPEs) through incorporation of Fe_3O_4 nanoparticles in the grafted poly(*n*-butyl acrylate-*co*-methyl methacrylate) [P(BA-*co*-MMA)] rubbery matrix. A broad spectrum of magnetic CTPEs can be fabricated by adjusting the composition of the grafted random copolymers and the content of Fe_3O_4 nanoparticles via this robust and effective synthetic strategy. The mechanical properties of the CTPEs were comprehensively investigated by monotonic and step cyclic tensile tests. The homogeneously dispersed Fe_3O_4 nanoparticles acting as multiple physical cross-linking points in the CTPEs strongly enhance the mechanical properties, such as higher tensile stress and elastic recovery. An in situ study on the microstructural evolution of the CTPEs during tensile deformation at room temperature was carried out to reveal the relationship between the microstructure and mechanical properties. The Fe_3O_4 nanoparticles are forced to be aligned along the tensile direction when the sample is extended, and the orientation degree increases as the strain increases, bringing out the strain-hardening behavior. The strain-hardening can be tailored by adjusting the content of incorporated Fe_3O_4 nanoparticles. These CTPEs are elastomeric polymer materials with strongly enhanced mechanical properties, excellent elastic recovery, and adjustable magnetic performance. The present work provides a new strategy to fabricate particular functional nanomaterials with controllable properties. The magnetic composite thermoplastic elastomers might have potential applications in robotic muscles and magnetic actuators.

ASSOCIATED CONTENT

Supporting Information

Additional experimental data as noted in the text. The Supporting Information is available free of charge on the ACS Publications website at DOI: 10.1021/acsami.5b02208.

AUTHOR INFORMATION

Corresponding Author

*Tel.: +86 0551-63607703. Fax: +86 0551-63607703. E-mail: zgwang2@ustc.edu.cn (Z.G.W.).

Notes

The authors declare no competing financial interest.

ACKNOWLEDGMENTS

Z.G.W. acknowledges financial support from the National Basic Research Program of China (Grant 2015CB351903) and the National Science Foundation of China (Grant 51473155). Prof. Yongfeng Men at Changchun Institute of Applied Chemistry, Chinese Academy of Sciences, is acknowledged for providing use of the SAXS facility.

REFERENCES

(1) MacLachlan, M. J.; Ginzburg, M.; Coombs, N.; Coyle, T. W.; Raju, N. P.; Greedan, J. E.; Ozin, G. A.; Manners, I. Shaped Ceramics with Tunable Magnetic Properties from Metal-Containing Polymers. *Science* **2000**, *287*, 1460−1463.

(2) Burke, N. A. D.; Stover, H. D. H.; Dawson, F. P. Magnetic Nanocomposites: Preparation and Characterization of Polymer-Coated Iron Nanoparticles. *Chem. Mater.* **2002**, *14*, 4752−4761.

(3) Podsiadlo, P.; Kaushik, A. K.; Arruda, E. M.; Waas, A. M.; Shim, B. S.; Xu, J. D.; Nandivada, H.; Pumplin, B. G.; Lahann, J.; Ramamoorthy, A.; Kotov, N. A. Ultrastrong and Stiff Layered Polymer Nanocomposites. *Science* **2007**, *318*, 80−83.

DOI: 10.1021/acsami.5b02208
ACS Appl. Mater. Interfaces 2015, 7, 10563−10575

(4) Garcia, I.; Tercjak, A.; Rueda, L.; Mondragon, I. Self-Assembled Nanomaterials Using Magnetic Nanoparticles Modified with Polystyrene Brushes and Poly(styrene-*b*-butadiene-*b*-styrene). *Macromolecules* **2008**, *41*, 9295−9298.
(5) Lee, H.; Lee, E.; Kim, D. K.; Jang, N. K.; Jeong, Y. Y.; Jon, S. Antibiofouling Polymer-Coated Superparamagnetic Iron Oxide Nanoparticles as Potential Magnetic Resonance Contrast Agents for in Vivo Cancer Imaging. *J. Am. Chem. Soc.* **2006**, *128*, 7383−7389.
(6) Yang, X. Q.; Pilla, S.; Grailer, J. J.; Steeber, D. A.; Gong, S. Q.; Chen, Y. H.; Chen, G. H. Tumor-Targeting, Superparamagnetic Polymeric Vesicles as Highly Efficient MRI Contrast Probes. *J. Mater. Chem.* **2009**, *19*, 5812−5817.
(7) Dong, H. C.; Mantha, V.; Matyjaszewski, K. Thermally Responsive $PM(EO)_2MA$ Magnetic Microgels via Activators Generated by Electron Transfer Atom Transfer Radical Polymerization in Miniemulsion. *Chem. Mater.* **2009**, *21*, 3965−3972.
(8) Xuan, S. H.; Wang, F.; Lai, J. M.; Sham, K. W.; Wang, Y. X. J.; Lee, S. F.; Yu, J. C.; Cheng, C. H.; Leung, K. C. F. Synthesis of Biocompatible, Mesoporous Fe_3O_4 Nano/Microspheres with Large Surface Area for Magnetic Resonance Imaging and Therapeutic Applications. *ACS Appl. Mater. Interfaces* **2011**, *3*, 237−244.
(9) Babic, M.; Horák, D.; Trchová, M.; Jendelová, P.; Glogarová, K.; Lesný, P.; Herynek, V.; Hájek, M.; Syková, E. Poly(L-lysine)-Modified Iron Oxide Nanoparticles for Stem Cell Labeling. *Bioconjugate Chem.* **2008**, *19*, 740−750.
(10) Gupta, A. K.; Gupta, M. Synthesis and Surface Engineering of Iron Oxide Nanoparticles for Biomedical Applications. *Biomaterials* **2005**, *26*, 3995−4021.
(11) Nam, J.-M.; Thaxton, C. S.; Mirkin, C. A. Nanoparticle-Based Bio-Bar Codes for the Ultrasensitive Detection of Proteins. *Science* **2003**, *301*, 1884−1886.
(12) Lu, A. H.; Salabas, E. e. L.; Schüth, F. Magnetic Nanoparticles: Synthesis, Protection, Functionalization, and Application. *Angew. Chem., Int. Ed.* **2007**, *46*, 1222−1244.
(13) Thévenot, J.; Oliveira, H.; Sandre, O.; Lecommandoux, S. Magnetic Responsive Polymer Composite Materials. *Chem. Soc. Rev.* **2013**, *42*, 7099−7116.
(14) Nguyen, V. Q.; Ahmed, A. S.; Ramanujan, R. V. Morphing Soft Magnetic Composites. *Adv. Mater.* **2012**, *24*, 4041−4054.
(15) Deplace, F.; Scholz, A. K.; Fredrickson, G. H.; Kramer, E. J.; Shin, Y. W.; Shimizu, F.; Zuo, F.; Rong, L. X.; Hsiao, B. S.; Coates, G. W. Tough and Elastic Thermoplastic Organogels and Elastomers Made of Semicrystalline Polyolefin-Based Block Copolymers. *Macromolecules* **2012**, *45*, 5604−5618.
(16) Liu, Y. P.; Yao, K. J.; Chen, X. M.; Wang, J. F.; Wang, Z. K.; Ploehn, H. J.; Wang, C. P.; Chu, F. X.; Tang, C. B. Sustainable Thermoplastic Elastomers Derived from Renewable Cellulose, Rosin and Fatty Acids. *Polym. Chem.* **2014**, *5*, 3170−3181.
(17) Jiang, F.; Zhang, Y. Q.; Fang, C.; Wang, Z. K.; Wang, Z. G. From Soft to Strong Elastomers: The Role of Additional Crosslinkings in Copolymer-Grafted Multiwalled Carbon Nanotube Composite Thermoplastic Elastomers. *RSC Adv.* **2014**, *4*, 60079−60085.
(18) Jiang, F.; Wang, Z. K.; Qiao, Y. L.; Wang, Z. G.; Tang, C. B. A Novel Architecture toward Third-Generation Thermoplastic Elastomers by a Grafting Strategy. *Macromolecules* **2013**, *46*, 4772−4780.
(19) Jiang, F.; Zhang, Y. Q.; Wang, Z. K.; Fang, H. G.; Ding, Y. S.; Xu, H. X.; Wang, Z. G. Synthesis and Characterization of Nanostructured Copolymer-Grafted Multiwalled Carbon Nanotube Composite Thermoplastic Elastomers toward Unique Morphology and Strongly Enhanced Mechanical Properties. *Ind. Eng. Chem. Res.* **2014**, *53*, 20154−20167.
(20) Wang, Z. K.; Jiang, F.; Zhang, Y. Q.; You, Y. Z.; Wang, Z. G.; Guan, Z. B. Bioinspired Design of Nanostructured Elastomers with Cross-Linked Soft Matrix Grafting on the Oriented Rigid Nanofibers To Mimic Mechanical Properties of Human Skin. *ACS Nano* **2015**, *9*, 271−278.
(21) Varga, Z.; Filipcsei, G.; Zrínyi, M. Smart Composites with Controlled Anisotropy. *Polymer* **2005**, *46*, 7779−7787.
(22) Razzaq, M. Y.; Anhalt, M.; Frormann, L.; Weidenfeller, B. Mechanical Spectroscopy of Magnetite Filled Polyurethane Shape Memory Polymers. *Mater. Sci. Eng., A* **2007**, *471*, 57−62.
(23) Nikitin, L. V.; Korolev, D. G.; Stepanov, G. V.; Mironova, L. S. Experimental Study of Magnetoelastics. *J. Magn. Magn. Mater.* **2006**, *300*, 234−238.
(24) Mietta, J. L.; Ruiz, M. M.; Antonel, P. S.; Perez, O. E.; Butera, A.; Jorge, G.; Negri, R. M. Anisotropic Magnetoresistance and Piezoresistivity in Structured Fe_3O_4−Silver Particles in Pdms Elastomers at Room Temperature. *Langmuir* **2012**, *28*, 6985−6996.
(25) Kumar, S. K.; Jouault, N.; Benicewicz, B.; Neely, T. Nanocomposites with Polymer Grafted Nanoparticles. *Macromolecules* **2013**, *46*, 3199−3214.
(26) Vestal, C. R.; Zhang, Z. J. Atom Transfer Radical Polymerization Synthesis and Magnetic Characterization of $MnFe_2O_4$/Polystyrene Core/Shell Nanoparticles. *J. Am. Chem. Soc.* **2002**, *124*, 14312−14313.
(27) Hu, F. X.; Neoh, K. G.; Cen, L.; Kang, E. T. Cellular Response to Magnetic Nanoparticles "PEGylated" Via Surface-Initiated Atom Transfer Radical Polymerization. *Biomacromolecules* **2006**, *7*, 809−816.
(28) Gelbrich, T.; Feyen, M.; Schmidt, A. M. Magnetic Thermoresponsive Core−Shell Nanoparticles. *Macromolecules* **2006**, *39*, 3469−3472.
(29) Xu, F.; Geiger, J. H.; Baker, G. L.; Bruening, M. L. Polymer Brush-Modified Magnetic Nanoparticles for His-Tagged Protein Purification. *Langmuir* **2011**, *27*, 3106−3112.
(30) Garcia, I.; Tercjak, A.; Zafeiropoulos, N. E.; Stamm, M.; Mondragon, I. Self-Assembling Nanomaterials Using Magnetic Nanoparticles Modified with Polystyrene Brushes. *Macromol. Rapid Commun.* **2007**, *28*, 2361−2365.
(31) Matyjaszewski, K.; Jakubowski, W.; Min, K.; Tang, W.; Huang, J. Y.; Braunecker, W. A.; Tsarevsky, N. V. Diminishing Catalyst Concentration in Atom Transfer Radical Polymerization with Reducing Agents. *Proc. Natl. Acad. Sci. U. S. A.* **2006**, *103*, 15309−15314.
(32) Nicolay, R.; Kwak, Y.; Matyjaszewski, K. A Green Route to Well-Defined High-Molecular-Weight (Co)Polymers Using ARGET ATRP with Alkyl Pseudohalides and Copper Catalysis. *Angew. Chem., Int. Ed.* **2010**, *49*, 541−544.
(33) Kwak, Y.; Magenau, A. J. D.; Matyjaszewski, K. ARGET ATRP of Methyl Acrylate with Inexpensive Ligands and ppm Concentrations of Catalyst. *Macromolecules* **2011**, *44*, 811−819.
(34) Wang, Z. K.; Zhang, Y. Q.; Jiang, F.; Fang, H. G.; Wang, Z. G. Synthesis and Characterization of Designed Cellulose-*graft*-polyisoprene Copolymers. *Polym. Chem.* **2014**, *5*, 3379−3388.
(35) Deng, H.; Li, X. L.; Peng, Q.; Wang, X.; Chen, J. P.; Li, Y. D. Monodisperse Magnetic Single-Crystal Ferrite Microspheres. *Angew. Chem., Int. Ed.* **2005**, *117*, 2842−2845.
(36) Huang, C.; Neoh, K. G.; Kang, E. T.; Shuter, B. Surface Modified Superparamagnetic Iron Oxide Nanoparticles (SPIONS) for High Efficiency Folate-Receptor Targeting with Low Uptake by Macrophages. *J. Mater. Chem.* **2011**, *21*, 16094−16102.
(37) Huang, C.; Neoh, K. G.; Kang, E.-T. Combined ATRP and 'Click' Chemistry for Designing Stable Tumor-Targeting Superparamagnetic Iron Oxide Nanoparticles. *Langmuir* **2011**, *28*, 563−571.
(38) Mukhopadhyay, A.; Joshi, N.; Chattopadhyay, K.; De, G. A Facile Synthesis of PEG-Coated Magnetite (Fe_3O_4) Nanoparticles and Their Prevention of the Reduction of Cytochrome C. *ACS Appl. Mater. Interfaces* **2011**, *4*, 142−149.
(39) Jakubowski, W.; Juhari, A.; Best, A.; Koynov, K.; Pakula, T.; Matyjaszewski, K. Comparison of Thermomechanical Properties of Statistical, Gradient and Block Copolymers of Isobornyl Acrylate and *n*-Butyl Acrylate with Various Acrylate Homopolymers. *Polymer* **2008**, *49*, 1567−1578.
(40) Cherifi, N.; Issoulie, A.; Khoukh, A.; Benaboura, A.; Save, M.; Derail, C.; Billon, L. Synthetic Methodology Effect on the Microstructure and Thermal Properties of Poly(*n*-butyl acrylate-*co*-methyl methacrylate) Synthesized by Nitroxide Mediated Polymerization. *Polym. Chem.* **2011**, *2*, 1769−1777.

DOI: 10.1021/acsami.5b02208
ACS Appl. Mater. Interfaces 2015, 7, 10563−10575

(41) Schlegel, R.; Duan, Y.; Weidisch, R.; Holzer, S.; Schneider, K.; Stamm, M.; Uhrig, D.; Mays, J.; Heinrich, G.; Hadjichristidis, N. High-Strain-Induced Deformation Mechanisms in Block-Graft and Multigraft Copolymers. *Macromolecules* **2011**, *44*, 9374−9383.
(42) Wang, W. W.; Wang, W. Y.; Lu, X. Y.; Bobade, S.; Chen, J. H.; Kang, N. G.; Zhang, Q. Y.; Mays, J. Synthesis and Characterization of Comb and Centipede Multigraft Copolymers PnBA-*g*-PS with High Molecular Weight Using Miniemulsion Polymerization. *Macromolecules* **2014**, *47*, 7284−7295.
(43) Moineau, C.; Minet, M.; Teyssié, P.; Jérôme, R. Synthesis and Characterization of Poly(methyl methacrylate)-*block*-poly(*n*-butyl acrylate)-*block*-poly(methyl methacrylate) Copolymers by Two-Step Controlled Radical Polymerization (ATRP) Catalyzed by $NiBr_2(PPh_3)_2$, 1. *Macromolecules* **1999**, *32*, 8277−8282.
(44) Tong, J. D.; Moineau, G.; Leclere, P.; Brédas, J. L.; Lazzaroni, R.; Jérôme, R. Synthesis, Morphology, and Mechanical Properties of Poly(methyl methacrylate)-*b*-poly(*n*-butyl acrylate)-*b*-poly(methyl methacrylate) Triblocks. Ligated Anionic Polymerization vs Atom Transfer Radical Polymerization. *Macromolecules* **2000**, *33*, 470−479.
(45) Matyjaszewski, K.; Shipp, D. A.; McMurtry, G. P.; Gaynor, S. G.; Pakula, T. Simple and Effective One-Pot Synthesis of (Meth)Acrylic Block Copolymers through Atom Transfer Radical Polymerization. *J. Polym. Sci., Part A: Polym. Chem.* **2000**, *38*, 2023−2031.
(46) Dufour, B.; Koynov, K.; Pakula, T.; Matyjaszewski, K. PBA-PMMA 3-Arm Star Block Copolymer Thermoplastic Elastomers. *Macromol. Chem. Phys.* **2008**, *209*, 1686−1693.
(47) Nese, A.; Mosnáček, J.; Juhari, A.; Yoon, J. A.; Koynov, K.; Kowalewski, T.; Matyjaszewski, K. Synthesis, Characterization, and Properties of Starlike Poly(*n*-butyl acrylate)-*b*-poly(methyl methacrylate) Block Copolymers. *Macromolecules* **2010**, *43*, 1227−1235.
(48) Haward, R.; Thackray, G. The Use of a Mathematical Model To Describe Isothermal Stress-Strain Curves in Glassy Thermoplastics. *Proc. R. Soc. London, Ser. A* **1968**, *302*, 453−472.
(49) Haward, R. Strain Hardening of Thermoplastics. *Macromolecules* **1993**, *26*, 5860−5869.
(50) Men, Y. F.; Rieger, J.; Strobl, G. Role of the Entangled Amorphous Network in Tensile Deformation of Semicrystalline Polymers. *Phys. Rev. Lett.* **2003**, *91*, 095502.
(51) Jancar, J.; Hoy, R. S.; Lesser, A. J.; Jancarova, E.; Zidek, J. Effect of Particle Size, Temperature, and Deformation Rate on the Plastic Flow and Strain Hardening Response of PMMA Composites. *Macromolecules* **2013**, *46*, 9409−9426.
(52) Bokobza, L.; Erman, B. A Theoretical and Experimental Study of Filler Effect on Stress-Deformation-Segmental Orientation Relations for Poly(dimethylsiloxane) Networks. *Macromolecules* **2000**, *33*, 8858−8864.
(53) Merabia, S.; Sotta, P.; Long, D. R. A Microscopic Model for the Reinforcement and the Nonlinear Behavior of Filled Elastomers and Thermoplastic Elastomers (Payne and Mullins Effects). *Macromolecules* **2008**, *41*, 8252−8266.
(54) Wang, Z. G.; Niu, Y. H.; Fredrickson, G. H.; Kramer, E. J.; Shin, Y. W.; Shimizu, F.; Zuo, F.; Rong, L. X.; Hsiao, B. S.; Coates, G. W. Step-Cycle Mechanical Processing of Gels of sPP-*b*-EPR-*b*-sPP Triblock Copolymer in Mineral Oil. *Macromolecules* **2010**, *43*, 6782−6788.
(55) Schneider, Y.; Lynd, N. A.; Kramer, E. J.; Bazan, G. C. Novel Elastomers Prepared by Grafting *n*-Butyl Acrylate from Polyethylene Macroinitiator Copolymers. *Macromolecules* **2009**, *42*, 8763−8768.
(56) Coffin, R. C.; Schneider, Y.; Kramer, E. J.; Bazan, G. C. Binuclear Initiators for the Telechelic Synthesis of Elastomeric Polyolefins. *J. Am. Chem. Soc.* **2010**, *132*, 13869−13878.
(57) Hong, K.; Rastogi, A.; Strobl, G. A Model Treating Tensile Deformation of Semicrystalline Polymers: Quasi-Static Stress−Strain Relationship and Viscous Stress Determined for a Sample of Polyethylene. *Macromolecules* **2004**, *37*, 10165−10173.
(58) Treloar, L. R. G. *The Physics of Rubber Elasticity*; Clarendon Press: Oxford, 1975.
(59) Nogales, A.; Sics, I.; Ezquerra, T. A.; Denchev, Z.; Balta Calleja, F. J.; Hsiao, B. S. In-Situ Simultaneous Small-and Wide-Angle X-ray Scattering Study of Poly(ether ester) During Cold Drawing. *Macromolecules* **2003**, *36*, 4827−4832.
(60) Hernández, J.; García-Gutiérrez, M. C.; Nogales, A.; Rueda, D. R.; Sanz, A.; Sics, I.; Hsiao, B. S.; Roslaniec, Z.; Broza, G.; Ezquerra, T. A. Deformation Behaviour During Cold Drawing of Nanocomposites Based on Single Wall Carbon Nanotubes and Poly(ether ester) Copolymers. *Polymer* **2007**, *48*, 3286−3293.
(61) Bitinis, N.; Sanz, A.; Nogales, A.; Verdejo, R.; Lopez-Manchado, M. A.; Ezquerra, T. A. Deformation Mechanisms in Polylactic Acid/Natural Rubber/Organoclay Bionanocomposites As Revealed by Synchrotron X-ray Scattering. *Soft Matter* **2012**, *8*, 8990−8997.
(62) Hernández, M.; Sanz, A.; Nogales, A.; Ezquerra, T. A.; López-Manchado, M. A. Structure and Segmental Dynamics Relationship in Natural Rubber/Layered Silicate Nanocomposites During Uniaxial Deformation. *Macromolecules* **2013**, *46*, 3176−3182.
(63) Saupe, A.; Maier, W. Methods for the Determination of the Degree of Order in Nematic Liquid-Crystal Layers. The Degree of Order of Azoxyanisole. *Z. Naturforsch., A: Phys., Phys. Phys. Chem.* **1961**, *16*, 816−824.
(64) Wang, Z. G.; Xia, Z. Y.; Yu, Z. Q.; Chen, E. Q.; Sue, H. J.; Han, C. C.; Hsiao, B. S. Lamellar Formation and Relaxation in Simple Sheared Poly(ethylene terephthalate) by Small-Angle X-ray Scattering. *Macromolecules* **2006**, *39*, 2930−2939.
(65) Valentín, J.; Mora Barrantes, I.; Carretero González, J.; López Manchado, M.; Sotta, P.; Long, D.; Saalwachter, K. Novel Experimental Approach To Evaluate Filler−Elastomer Interactions. *Macromolecules* **2009**, *43*, 334−346.

DOI: 10.1021/acsami.5b02208
ACS Appl. Mater. Interfaces 2015, 7, 10563−10575